



Cite this: *Lab Chip*, 2020, 20, 995

Aberration-free aspherical in-plane tunable liquid lenses by regulating local curvatures†

Qingming Chen,^a Xiliang Tong,^b Yujiao Zhu,^a Chi Chung Tsoi,^b Yanwei Jia,^{cde} Zhaohui Li^{fg} and Xuming Zhang^{id*acg}

Aberration is a long-standing problem of fixed focal lenses and a complicated lens set is usually required to compensate for aberration. It becomes more challenging for tunable lenses. This paper reports an original design of an in-plane optofluidic lens that enables compensation for spherical aberration during the tuning of focal length. The key idea is to use two arrays of electrode strips to symmetrically control the two air/liquid interfaces by the dielectrophoretic effect. The strips work together to define the global shape of the lens interface and thus the focal length, whereas each strip regulates the local curvature of the interface to focus the paraxial and peripheral arrays on the same point. Experiments using a silicone oil droplet demonstrate the tuning of focal length over 500–1400 μm and obtain a longitudinal spherical aberration (LSA) of $\sim 3.5 \mu\text{m}$, which is only 1/24 of the LSA (85 μm) of the spherical lens. Fine adjustment of the applied voltages of strips allows even elimination of the LSA and enabling of the aberration-free tunable lenses. It is the first time that local curvature regulation is used to compensate for the aberration within one in-plane liquid lens. This simple and effective method will find potential applications in lab-on-a-chip systems.

Received 11th December 2019,
Accepted 31st January 2020

DOI: 10.1039/c9lc01217f

rsc.li/loc

Introduction

Optofluidics combines microfluidics and optics to exert the advantages of both and has demonstrated unprecedented features such as large tunability, high compatibility and multi-functionality in various devices and systems.^{1–7} Among them, tunable liquid lenses with small size and tunable focal length have attracted intensive attention.^{8–10} In general, the focal length is tuned by changing either the refractive index profile^{11,12} or the fluidic interface of the liquid lens.^{13–21} The former mostly utilizes miscible liquids and relies on the fine control of their diffusion,^{12,22} which is complicated but can generate advanced optical field patterns.²³ The latter exploits immiscible liquids and modulates their interfaces by many

actuation mechanisms such as pneumatic/hydrodynamic pressure,²⁴ electrowetting (EW),^{14,21,25–27} dielectrophoresis (DEP),^{19,28–31} and so on. Among them, the DEP method makes use of the electrical field and is favorable for lab-on-a-chip integration in view of its unique merits such as small size, easy fabrication and static liquid flow (*i.e.*, avoiding the need of continuous liquid supply). It also enables fast response (~ 1 ms) and wide tunability of the focal length (*e.g.*, from negative to infinite and then to positive).^{32,33} In addition, electrically actuated liquid lenses usually have high reliability and long lifetime since they require no mechanical moving parts.

In reported tunable liquid lenses, most of them manipulate the global curvature of interfaces and preserve the spherical shapes.^{8,34} Therefore, spherical aberration becomes inevitable, causing poor imaging quality. In in-plane liquid lenses, the difference between the focal lengths of the peripheral and paraxial rays results in longitudinal spherical aberration (LSA). In the conventional bulky optical systems, the aberration is compensated by a multiple-lens system. But in microfluidic chips, it is difficult to precisely control several individual lenses. Therefore, the manipulation of local curvatures is a feasible way to achieve aberration-free systems.

Various mechanisms have been proposed to realize out-of-plane aspherical optofluidic lenses.³⁵ One simple and direct method is to use pre-molded membranes^{36–38} or non-circular apertures³⁹ to modulate the asphericity of the liquid lenses. Among them, the use of electrostatic force has been proved

^a Department of Applied Physics, The Hong Kong Polytechnic University, Hong Kong, China. E-mail: apzhang@polyu.edu.hk

^b Beijing Institute of Space Mechanics & Electricity, Beijing 100094, China

^c State Key Laboratory of Analog and Mixed Signal VLSI, Institute of Microelectronics, University of Macau, Macau, China

^d Faculty of Science and Technology, University of Macau, Macau, China

^e Faculty of Health Sciences, University of Macau, Macau, China

^f School of Electronics and Information Engineering, State Key Laboratory of Optoelectronic Materials and Technologies, Sun Yat-sen University, Guangzhou 510275, China

^g Southern Marine Science and Engineering Guangdong Laboratory (Zhuhai), Zhuhai, China

† Electronic supplementary information (ESI) available. See DOI: 10.1039/c9lc01217f

to be a much more practical method since it does not require complicated fabrication and provides flexible tunability of the focal length. Zhan *et al.* demonstrated an electrostatically induced aspherical lens, which was distorted from an initially spherical to parabolic and to a nearly conical shape.⁴⁰ Mugele's group has extensively explored the tuning of aspherical lenses by the combination of hydrostatic pressure and electrostatic force.^{41–44} By using a 10×10 array of individually addressable electrodes, they demonstrated the tuning of different types of optical aberrations such as horizontal astigmatism, oblique astigmatism, coma and spherical aberrations.⁴¹ In that work, a spherical surface with a constant curvature R was induced by the hydrostatic pressure at first. Then different voltages were applied to the discrete electrodes to generate a complicated electric field distribution, which finely tuned the lens shapes.

While the previous methods mainly deal with out-of-plane lenses, the aberration control of in-plane optofluidic lenses is still lacking. The in-plane optofluidic lens plays an important role in light manipulation and coupling inside the microfluidic chips, in which the spherical aberration is critical.³⁴ Recently, we demonstrated dielectrophoresis-actuated in-plane optofluidic lenses with one³³ or two³² air/liquid interfaces. Although the two electrodes enabled the individual tuning of the two air/liquid interfaces, the spherical shapes were preserved. In this type of lens, the peripheral rays are focused closer to the lens, resulting in the defocusing of off-axis rays and thus the poor quality of the focused beam. Therefore, spherical aberration-free in-plane lenses are urgently needed.

In this work, we propose to regulate the local curvatures of an in-plane liquid lens. Two electrode arrays, each of which consists of several separated electrode strips, are used to modulate the air/liquid interfaces. The independent control of each electrode makes it easy to tune the air/liquid

interfaces to an arbitrary aspherical shape, enabling elimination of the spherical aberration of the in-plane optofluidic lenses. Numerical simulation and experimental ray tracing both verify that the focusing quality can be improved significantly.

Working principle

In conventional optical systems, spherical lenses are the most popular due to their easy and mature fabrication techniques. In the spherical lens, there is a longitudinal shift between the focal points of the peripheral and paraxial rays (see the blue rays in Fig. 1a). It reduces the imaging quality of the optical system. To focus the peripheral rays on the focal point of the paraxial rays, the peripheral section should have a smaller local curvature compared with the paraxial section of the lens. In a well-designed aspherical lens, all the rays are well focused on a point (see the black rays in Fig. 1a). In the past, it is difficult to fabricate such an aspherical lens. Now, the development of microfluidics makes it possible to manipulate the local curvatures of lenses. For instance, the interface of the lens can be divided into discrete slices, which are manipulated independently (see Fig. 1b). In this way, the local curvatures along the interface can be freely regulated, making it easy to obtain any aspherical shape of the lens interfaces.

Inspired by the idea in Fig. 1b, we propose to manipulate the local curvatures of the air/liquid interfaces using the DEP effect. The 3D schematic design is illustrated in Fig. 1c. Two glass plates are bonded together by four polymer strips (Norland Optical Adhesive 81, NOA 81). Between the two plates (spacing $H_0 = 50 \mu\text{m}$), a silicone oil droplet is sandwiched at the center and surrounded by air to form a lens. On the top plate, two arrays of ITO strips are coated for electrical driving. The width of the strip is $40 \mu\text{m}$, and the distance between the two adjacent strips is $115 \mu\text{m}$. The non-

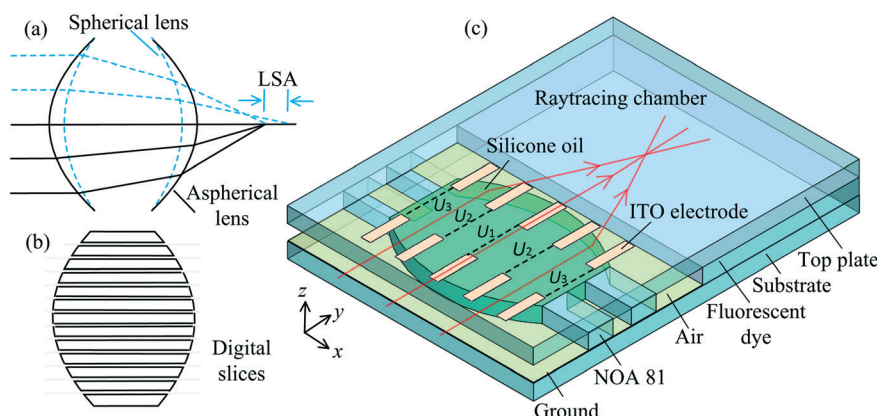


Fig. 1 Working principle of the control of longitudinal spherical aberration (LSA). (a) In the spherical lens (blue dashed lines), the peripheral rays have a shorter focal length than the paraxial rays, causing a shift between the focal points thus resulting in the LSA. In the aspherical lens (black solid lines), all the rays are focused on a single point, resulting in no LSA. (b) The lens interfaces are divided into discrete slices with variable local curvatures to form an aspherical lens. (c) Schematic design of the DEP-actuated aspherical lens. An ITO layer is coated on the substrate as the ground. The external voltages are applied to the lens by two arrays of ITO electrode strips patterned on the top plate. U_i denotes the voltages of the i th electrode strip (here $i = 1, 2, 3, \dots$). The two air/liquid interfaces are loaded symmetrically. The probe laser beam is coupled into the chip with a fiber lens (not shown here). A ray tracing chamber is positioned after the lens to visualize the focusing effect.

patterned ITO film on the bottom plate acts as the ground. During the tuning process, the edges of the droplet are pinned to the NOA 81 ridges whereas the local curvatures of the lens interfaces are regulated by the applied voltages. A fiber lens is used to couple the probe laser beam (collimated, beam diameter = 400 μm , $\lambda = 532 \text{ nm}$) into the microfluidic chip. To visualize the optical paths of the rays, a ray tracing chamber filled with Rhodamine B dye (dissolved in NOA 81) is fabricated on the other side of the lens.

According to Laplace's law, the air/liquid interface remains spherical when it is at the mechanical equilibrium without any external perturbation. The global shape is determined by the pressure drop across the interface as governed by:⁴⁵

$$\Delta P_0 = 2\gamma\kappa_0 = \gamma\left(\frac{1}{R_{10}} + \frac{1}{R_{20}}\right) \quad (1a)$$

$$\Delta P_1 = 2\gamma\kappa_1 = \gamma\left(\frac{1}{R_{11}} + \frac{1}{R_{20}}\right) \quad (1b)$$

where ΔP is the pressure drop, $\gamma = 20 \text{ mN m}^{-1}$ is the surface tension coefficient of the silicone oil/air interface and κ is the mean curvature, respectively. R_{10} (in the horizontal direction) and R_{20} (in the vertical direction) are the principal curvature radii at the interface. In the initial balanced state, the spherical air/liquid interface results from the surface tension. Then, the external voltages are applied to the two electrode arrays to exert the DEP forces at different locations of the air/liquid interfaces. And the horizontal curvature radius is changed from R_{10} to R_{11} . The DEP force of each electrode strip can be expressed as:^{46,47}

$$F_i = \frac{\varepsilon_0(\varepsilon_L - 1)W_0}{2H_0} U_i^2 \quad (2)$$

where $\varepsilon_0 = 8.8542 \times 10^{-12} \text{ F m}^{-1}$ is the permittivity of vacuum, $\varepsilon_L = 2.5$ is the relative permittivity of the silicone oil, $W_0 = 40 \mu\text{m}$ is the width of the electrode strip and $H_0 = 50 \mu\text{m}$ is the height of the microchamber. U_i represents the voltage applied to the i th electrode (here $i = 1, 2, 3, \dots$). Under the influence of the DEP force, the silicone oil tends to collectively accumulate to the section with a stronger electric field. When different voltages are applied to the different electrode strips to generate a nonuniform electrical field, the local curvatures at different sections of the air/liquid interfaces can be regulated, making it possible to eliminate the spherical aberration of the liquid lens.

Tuning of the focal length by modulating the global shape of interfaces

There are two experimental methods to demonstrate the tunability of the liquid lens. One is to modulate the shape of the lens. Another one is using the experimental ray tracing. Here the above two methods are combined to demonstrate the reconfigurability of the lens.

Ray tracing is the most straightforward method to demonstrate the lensing effect. For this purpose, a ray tracing

chamber filled with Rhodamine B is used for fluorescence imaging (see Fig. 2). In the experiment, the device is connected to three independent electrical drivers to apply voltages U_1 , U_2 and U_3 (see Fig. 1c). At first, the external voltages are increased gradually to turn the droplet into a biconvex shape. Then, the voltages are precisely controlled to finely adjust the air/liquid interfaces into an aspherical shape. Three different working states are shown in Fig. 2. As seen from the optical images of the liquid lens (the left column of Fig. 2), the global shape of the air/liquid interfaces is modulated in response to the change of applied voltages. With $U_1 = 270$, $U_2 = 275 \text{ V}$ and $U_3 = 200 \text{ V}$, a biconvex lens with a slight bump is obtained to have a focal length of 1335 μm , as visualized by the fluorescence image in the right column of Fig. 2a. When U_2 is increased to 280 V, the focal length is shortened to 1061 μm (see Fig. 2b). To further increase the global curvature of the lens, we increase the voltages at the central section and reduce those at the peripheral section at the same time. In this way, the global curvature of the air/liquid interface is increased significantly. At $U_1 = 290 \text{ V}$, $U_2 = 295 \text{ V}$ and $U_3 = 190 \text{ V}$, the droplet becomes a highly convergent lens as shown in Fig. 2c. The beam has been tightly focused into a bright spot with a focal length of about 592 μm . The above lensing states well demonstrate the tuning of the focal length.

Suppression of longitudinal spherical aberration (LSA) by regulating the local curvatures of interfaces

The aberration and focusing performance of the lens are usually evaluated by interferometric characterization, which is based on the Mach-Zehnder interferometer.⁴⁸ The optical properties of the lens are recorded by the interference pattern. For instance, the aberrations of the lens can be

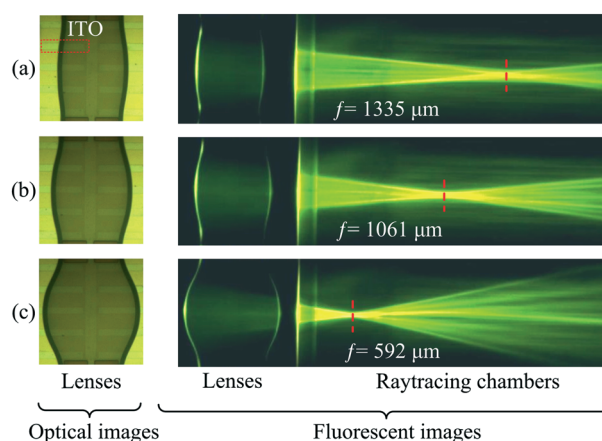


Fig. 2 Tuning of the focal length of the liquid lens using the discrete electrode strips. The left column shows the air/liquid interfaces and the right side shows the corresponding experimental ray tracing. Biconvex lenses have (a) $f = 1335 \mu\text{m}$ when $U_1 = 270$, $U_2 = 275 \text{ V}$ and $U_3 = 200 \text{ V}$; (b) $f = 1061 \mu\text{m}$ when $U_1 = 270 \text{ V}$, $U_2 = 280 \text{ V}$ and $U_3 = 200 \text{ V}$; (c) $f = 592 \mu\text{m}$ when $U_1 = 290 \text{ V}$, $U_2 = 295 \text{ V}$ and $U_3 = 190 \text{ V}$. The red frame in (a) exemplifies one of the ITO electrode strips.

extracted from a phase map. However, the in-plane liquid lens is integrated inside a microfluidic chip, in which the beam is confined and propagated. Therefore, it is difficult to obtain a digital hologram inside the chip. In this work, the optical performance of the lens is evaluated by numerical ray tracing and fluorescence imaging.

To suppress the LSA of the in-plane liquid lens, the local curvature of the air/liquid interface is regulated by finely tuning the voltages. In the following section, both the numerical and experimental ray tracing studies will be conducted to verify this idea. Here the LSA is defined as $LSA = f_{\text{paraxial}} - f_{\text{peripheral}}$, where f_{paraxial} and $f_{\text{peripheral}}$ are the focal lengths of the paraxial rays and the peripheral rays, respectively. With this definition, the value of LSA could be positive, 0 or negative.

The numerical ray tracing of the two lenses are shown in Fig. 3, in which the lens shapes are captured from the experiments. At $U_1 = 277$ V, $U_2 = 300$ V and $U_3 = 190$ V, the liquid lens is spherical (see Fig. 3a). It has a mean curvature radius of $406\text{ }\mu\text{m}$ and a paraxial focal length of $609.6\text{ }\mu\text{m}$. The peripheral rays are focused closer to the lens, leading to a positive value of $LSA = 49.6\text{ }\mu\text{m}$. To suppress the aberration, the lens should have a larger local curvature at the central section to shorten the focal length of the paraxial rays. For this purpose, we increase the value of U_1 from 277 to 290 V and reduce U_2 from 300 to 295 V, thereby increasing the local curvature of the central section. As shown in Fig. 3b, the shape of the lens interface is slightly shifted away from the spherical one (red dashed curve in Fig. 3b), and the center has the highest local curvature. It is easy to see that all the rays are well focused on the same focal point, with $LSA = 2.3\text{ }\mu\text{m}$ (only 4.6% of the spherical lens $LSA = 49.6\text{ }\mu\text{m}$). The above analysis verifies that this lens design can significantly suppress the LSA. Further fine adjustment of the voltages can even eliminate the LSA, achieving the aberration-free focusing during the tuning of focal length.

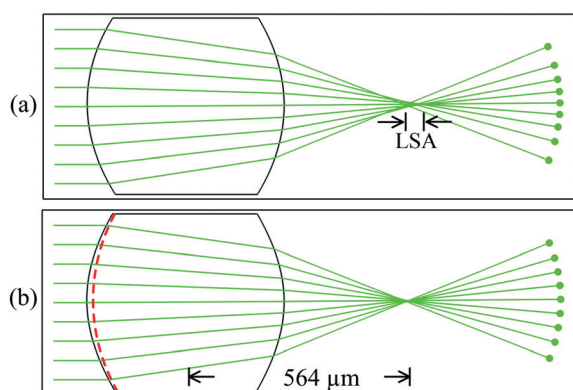


Fig. 3 Calculated ray tracing of the experimentally obtained air/liquid interfaces. (a) At $U_1 = 277$ V, $U_2 = 300$ V and $U_3 = 190$ V, the lens has spherical interfaces ($R = 406\text{ }\mu\text{m}$, $f = 609.6\text{ }\mu\text{m}$) with $LSA = 49.6\text{ }\mu\text{m}$; (b) by increasing the voltages of the paraxial section ($U_1 = 290$ V, $U_2 = 295$ V, $U_3 = 190$ V), the lens becomes aspherical and the beam is tightly focused ($f = 564\text{ }\mu\text{m}$, $LSA = 2.3\text{ }\mu\text{m}$). The red dashed curve in (b) indicates the spherical interface of the lens in (a).

To experimentally demonstrate aberration control ability, the focal lengths of both the paraxial and peripheral rays are manipulated independently. Fig. 4a shows the focal state of the spherical lens ($U_1 = 277$ V, $U_2 = 300$ V and $U_3 = 190$ V). As the peripheral and paraxial rays are not focused together, the focal point is not clear. In particular, the peripheral rays are focused closer to the lens, resulting in a positive LSA ($L_1 = 76\text{ }\mu\text{m}$). By increasing the local curvature of the central section ($U_1 = 290$ V, $U_2 = 295$ V and $U_3 = 190$ V), the focal point of the paraxial rays is shifted towards that of the peripheral rays, resulting in a sharp and clear focus at $f = 592\text{ }\mu\text{m}$ (see Fig. 4b). In Fig. 4(c), the local curvature of the peripheral section is higher ($U_1 = 265$ V, $U_2 = 290$ V and $U_3 = 200$ V), leading to a shorter focal length of the peripheral section ($f_{\text{paraxial}} = 1058\text{ }\mu\text{m}$, $f_{\text{peripheral}} = 855\text{ }\mu\text{m}$) and thus a positive LSA $203\text{ }\mu\text{m}$. Then we try to reduce the curvature of the peripheral section, thereby moving the peripheral focal point to the paraxial focal point. In Fig. 4d, the peripheral focal point is shifted to the paraxial focal point to achieve a better focused beam ($U_1 = 270$ V, $U_2 = 280$ V, $U_3 = 200$ V, and $f = 1061\text{ }\mu\text{m}$). These experiments verify that the design can compensate for both the positive and negative LSAs, thereby suppressing or even eliminating the aberration.

In this work, the lensing effect is measured by fluorescence imaging. A CCD camera is used to capture the fluorescence images, which are then used to analyze the focusing performance of the lens. The accuracy of this method is limited to $\sim 3\text{ }\mu\text{m}$. Although the evaluation is not as good as that of the interferometer, it has successfully demonstrated the aberration suppression of this lens. And

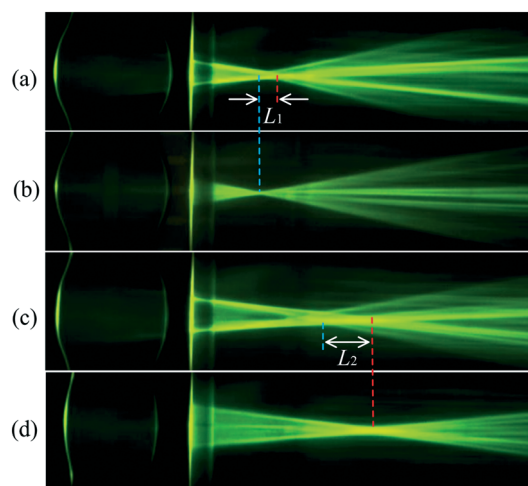


Fig. 4 Experimental results of aberration control. The blue and red dashed lines indicate the focal points of the peripheral and paraxial rays, respectively. (a) and (b) are the measured lens states corresponding to those in Fig. 3. Here (a) $U_1 = 277$ V, $U_2 = 300$ V, $U_3 = 190$ V and $f_{\text{paraxial}} = 663\text{ }\mu\text{m}$, $f_{\text{peripheral}} = 587\text{ }\mu\text{m}$, $L_1 = 76\text{ }\mu\text{m}$, (b) $U_1 = 290$ V, $U_2 = 295$ V, $U_3 = 190$ V and $f = 592\text{ }\mu\text{m}$. Next, by tuning the voltages from (c) $U_1 = 265$ V, $U_2 = 290$ V, $U_3 = 200$ V and $f_{\text{paraxial}} = 1058\text{ }\mu\text{m}$, $f_{\text{peripheral}} = 855\text{ }\mu\text{m}$, $L_2 = 203\text{ }\mu\text{m}$ to (d) $U_1 = 270$ V, $U_2 = 280$ V, $U_3 = 200$ V and $f = 1061\text{ }\mu\text{m}$, the focal point of the peripheral rays approaches that of the paraxial rays to suppress the LSA.

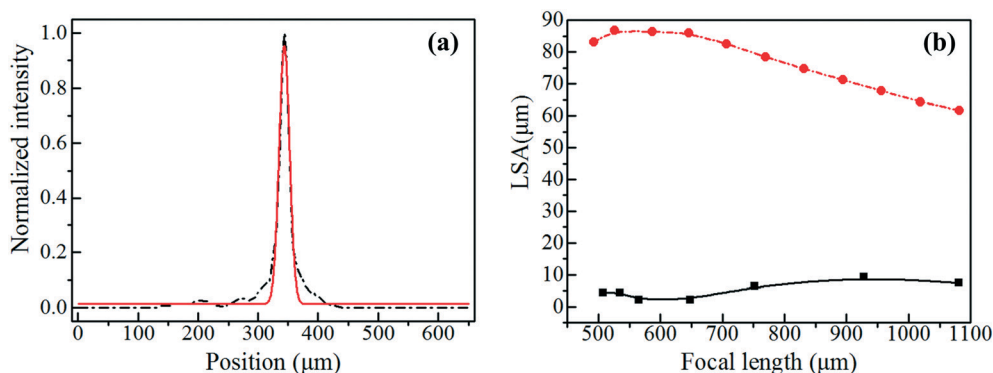


Fig. 5 (a) The Gaussian fitting (red solid line) of the normalized intensity profile (black dash-dotted line) of the focal point in Fig. 4b. (b) The comparison between the LSA of the spherical lens (red) and the experimental results (the magnitude, black) of our lens design.

the results are consistent with the numerical ray tracing analysis in Fig. 3. In addition, the results in Fig. 4 shows that the lens is capable of continuously tuning the LSA from positive to negative. Therefore, the fluorescence imaging measurement is acceptable in this work.

The intensity profile of the focal point in Fig. 4b is normalized and plotted in Fig. 5a (the black dash-dotted line). It is well fitted by the Gaussian function (red solid line), exhibiting a sharp peak at the center. This further proves that the focal quality is high. For comparison, the LSA of the spherical lens and the measured LSA (the magnitude) of our lens design are plotted in Fig. 5b. The spherical lens has a positive LSA of 70–90 μm when the focal length is tuned over $f = 500$ –1100 μm. In contrast, the measured LSA of our design is always <10 μm. Particularly, we have successfully suppressed the LSA to ~ 3.5 μm when $f = 500$ to 700 μm, whereas that of the spherical lens is ~ 85 μm. The suppression ratio is ~ 24 . It is worth mentioning that some cases in our experiments show a negative LSA. For instance, when the driving voltages are varied from $U_1 = 295$ V, $U_2 = 305$ V and $U_3 = 170$ V to $U_1 = 295$ V, $U_2 = 300$ V and $U_3 = 170$ V, the LSA is changed from 4.4 to -4.5 μm. Therefore, a carefully designed discrete electrode array would be able to eliminate the LSA in a single lens.

Conclusions

This paper presents a unique design of an in-plane optofluidic lens that utilizes two arrays of electrode strips. The strips work together to define the global shape of the air/liquid interfaces while each strip is driven independently to regulate the local curvatures of a section of the lens interface. The tuning of the global shape facilitates the wide tuning of focal length, and the regulation of local curvatures enables significant suppression or even elimination of the LSA. Numerical and experimental ray tracing studies have been conducted to verify the above idea. Due to the large size of the lens and the edge pinning effect, the response speed of the lens is slow. It takes about 6 seconds to stabilize the lens at the tightly focused state. And the response time of the

aberration modulation is ~ 0.1 s. The response speed can be improved by either reducing the size or using a liquid with lower viscosity. The superior performance of this aberration-free liquid lens would find niche applications in lab-on-a-chip systems, such as optical imaging, particle trapping/sorting, optical sensing and optical switching. In addition, the manipulation of the local curvature would be used to control the wavefront of light.

Materials and methods

Device fabrication

The devices are fabricated in the UMF (University Research Facility in Materials Characterization and Device Fabrication) of the Hong Kong Polytechnic University by photolithography, film deposition, *etc.* The substrate and the top plate with ITO (indium tin oxide) electrode strips are bonded together by a home-made process using NOA 81 (Norland Optical Adhesive 81).

The ITO strips on the top glass are prepared by a lift-off process. The first step is to fabricate sacrificial photoresist patterns on the glass using photolithography. The glass is cleaned with acetone, isopropanol, ethanol and distilled water using ultrasonication in sequence. An AZ5214 photoresist layer with a thickness of 2 μm is spin coated onto the glass and then baked at 110 °C for 3 minutes. After that, UV (365 nm) exposure is used to transfer the mask patterns into the photoresist layer. The sample is immersed in the developer for 20 seconds to dissolve the exposed photoresist. The second step is film deposition, in which an ITO thin film layer is deposited on the above glass by sputtering at room temperature. Then the sample is immersed in acetone for 5 hours to remove the unwanted area, leaving the ITO strips on the glass. To make the ITO conductive, the sample is put on a hotplate at 300 °C for 3 hour annealing.

The device is bonded by a home-made process. A PDMS (polydimethylsiloxane) mold is prepared by the conventional SU8 50 photolithography (Micro Chem). Then, the mold is brought into contact with clean ITO glass, forming a temporary microfluidic channel that is predefined on the

PDMS surface. A droplet of NOA 81 is placed at the inlet of the channel, which will guide the droplet moving along the predefined path by capillary. The channel filled with NOA 81 can be cured by 5 minutes of UV exposure. By peeling the PDMS mold away, the NOA 81 spacer with a height of 50 μm is left on the substrate. As there is a very thin (~ 100 nm) active film on the NOA 81 spacer, it can be used to bond the top and bottom glasses together by another 3 minutes of UV exposure.

Experimental measurement

To experimentally observe the optical path inside the microfluidic chip, the ray tracing chamber is filled with Rhodamine B dye, which emits fluorescence (it absorbs 532 nm light and emits 580 nm fluorescence) for CCD imaging. The collimated laser ($\lambda = 532$ nm, waist = 400 μm , power = 5 mW) is coupled into the chip as the probe beam. Three DC drivers, which have a tunable output in the range of 0–500 V, are used to control the microfluidic chip. A droplet of silicone oil is placed into the chip and modulated by the applied DEP force to form the reconfigurable liquid lens. During the experiment, a long pass filter is used to cut off the light below 550 nm. Some pictures and videos of the experiments are captured using the CCD for post processing.

Author's contributions

X. Z. led this work. Q. C. and Y. Z. fabricated the devices. Q. C. and C. C. T. built the experimental setup and conducted the experimental measurements. Q. C. and X. T. performed the data processing and theoretical analysis. Q. C. and Z. L. prepared the manuscript. Y. J. and X. Z. revised the paper.

Conflicts of interest

There are no conflicts of interest to declare.

Acknowledgements

X. Z. acknowledges the Hong Kong Research Grant Council (Grant No. 152184/15E, 152127/17E, 152126/18E and 152219/19E) and The Hong Kong Polytechnic University (Grant No. 1-ZE14, 1-ZE27 and 1-ZVGH). The technical assistance and facility support from the Materials Research Centre and the University Research Facility in Material Characterization and Device Fabrication of The Hong Kong Polytechnic University are also acknowledged.

References

- 1 D. Psaltis, S. R. Quake and C. Yang, *Nature*, 2006, **442**, 381–386.
- 2 C. Monat, P. Domachuk and B. J. Eggleton, *Nat. Photonics*, 2007, **1**, 106–114.
- 3 G. W. Whitesides, *Nature*, 2006, **442**, 368–373.
- 4 D. Erickson, D. Sinton and D. Psaltis, *Nat. Photonics*, 2011, **5**, 583–590.
- 5 H. Schmidt and A. R. Hawkins, *Nat. Photonics*, 2011, **5**, 598–604.
- 6 X. Fan and S.-H. Yun, *Nat. Methods*, 2014, **11**, 141–147.
- 7 X. Fan and I. M. White, *Nat. Photonics*, 2011, **5**, 591–597.
- 8 N. T. Nguyen, *Biomicrofluidics*, 2010, **4**, 031501.
- 9 C. P. Chiu, T. J. Chiang, J. K. Chen, F. C. Chang, F. H. Ko, C. W. Chu, S. W. Kuo and S. K. Fan, *J. Adhes. Sci. Technol.*, 2012, **26**, 1773–1788.
- 10 S. Camou, H. Fujita and T. Fujii, *Lab Chip*, 2003, **3**, 40–45.
- 11 Q. Chen, A. Jian, Z. Li and X. M. Zhang, *Lab Chip*, 2016, **16**, 104–111.
- 12 X. Mao, S. C. S. Lin, M. I. Lapsley, J. Shi, B. K. Juluri and T. J. Huang, *Lab Chip*, 2009, **9**, 2050–2058.
- 13 J. Shi, Z. Stratton, S.-C. S. Lin, H. Huang and T. J. Huang, *Microfluid. Nanofluid.*, 2009, **9**, 313–318.
- 14 B. H. W. Hendriks, S. Kuiper, M. A. J. VAN As, C. A. Renders and T. W. Tukker, *Opt. Rev.*, 2005, **12**, 255–259.
- 15 Y. C. Seow, A. Q. Liu, L. K. Chin, X. C. Li, H. J. Huang, T. H. Cheng and X. Q. Zhou, *Appl. Phys. Lett.*, 2008, **93**, 084101.
- 16 J.-M. Lim, J. P. Urbanski, T. Thorsen and S.-M. Yang, *Appl. Phys. Lett.*, 2011, **98**, 044101.
- 17 C.-C. Cheng, C. A. Chang and J. A. Yeh, *Opt. Express*, 2006, **14**, 4101–4106.
- 18 X. Mao, J. R. Waldeisen, B. K. Juluri and T. J. Huang, *Lab Chip*, 2007, **7**, 1303–1308.
- 19 C.-C. Cheng and J. A. Yeh, *Opt. Express*, 2007, **15**, 7140–7145.
- 20 H. Li, C. Song, T. D. Luong, N.-T. Nguyen and T. N. Wong, *Lab Chip*, 2012, **12**, 3680–3687.
- 21 S. Kuiper and B. H. W. Hendriks, *Appl. Phys. Lett.*, 2004, **85**, 1128–1130.
- 22 Y. Yang, L. K. Chin, J. M. Tsai, D. P. Tsai, N. I. Zheludev and A. Q. Liu, *Lab Chip*, 2012, **12**, 3785–3790.
- 23 Y. Yang, A. Q. Liu, L. K. Chin, X. M. Zhang, D. P. Tsai, C. L. Lin, C. Lu, G. P. Wang and N. I. Zheludev, *Nat. Commun.*, 2012, **3**, 651.
- 24 C. Fang, B. Dai, Q. Xu, R. Zhuo, Q. Wang, X. Wang and D. Zhang, *Opt. Express*, 2017, **25**, 888–897.
- 25 F. Mugele and J.-C. Baret, *J. Phys.: Condens. Matter*, 2005, **17**, R705–R774.
- 26 P. Ferraro, S. Grilli, L. Miccio and V. Vespini, *Appl. Phys. Lett.*, 2008, **92**, 213107.
- 27 S. Grilli, L. Miccio, V. Vespini, A. Finizio, S. De Nicola and P. Ferraro, *Opt. Express*, 2008, **16**, 8084–8093.
- 28 T. B. Jones, *Langmuir*, 2002, **18**, 4437–4443.
- 29 S. Xu, H. Ren and S.-T. Wu, *J. Phys. D: Appl. Phys.*, 2013, **46**, 483001.
- 30 H. Ren and S.-T. Wu, *Opt. Express*, 2008, **16**, 2646–2652.
- 31 S. Xu, Y.-J. Lin and S.-T. Wu, *Opt. Express*, 2009, **17**, 10499–10505.
- 32 Q. Chen, T. Li, Z. Li, C. Lu and X. M. Zhang, *Lab Chip*, 2018, **18**, 3849–3854.
- 33 Q. Chen, T. Li, Y. Zhu, W. Yu and X. M. Zhang, *Opt. Express*, 2018, **26**, 6532–6541.
- 34 Q. Chen, T. Li, Z. Li, J. Long and X. M. Zhang, *Micromachines*, 2018, **9**, 97.

- 35 K. Mishra, D. V. D. Ende and F. Mugele, *Micromachines*, 2016, **7**, 102.
- 36 H. Yu, G. Zhou, H. M. Leung and F. S. Chau, *Opt. Express*, 2010, **18**, 9945–9954.
- 37 P. Zhao, C. Ataman and H. Zappe, *Opt. Express*, 2015, **23**, 21264–21278.
- 38 K. Wei, H. Huang, Q. Wang and Y. Zhao, *Opt. Express*, 2016, **24**, 3929–3939.
- 39 Y. K. Fuh and C. T. Huang, *Opt. Commun.*, 2014, **323**, 148–153.
- 40 Z. Zhan, K. Wang, H. Yao and Z. Cao, *Appl. Opt.*, 2009, **48**, 4375–4380.
- 41 N. C. Lima, K. Mishra and F. Mugele, *Opt. Express*, 2017, **25**, 6700–6711.
- 42 K. Mishra, C. Murade, B. Carreel, I. Roghair, J. M. Oh, G. Manukyan, D. V. D. Ende and F. Mugele, *Sci. Rep.*, 2014, **4**, 6378.
- 43 N. C. Lima, A. Cavalli, K. Mishra and F. Mugele, *Opt. Express*, 2016, **24**, 4210–4220.
- 44 K. Mishra, A. Narayanan and F. Mugele, *Opt. Express*, 2019, **27**, 17601–17609.
- 45 L. Hu, M. Wu, W. Chen, H. Xie and X. Fu, *Exp. Therm. Fluid Sci.*, 2017, **87**, 50–59.
- 46 S. K. Fan, T. H. Hsieh and D. Y. Lin, *Lab Chip*, 2009, **9**, 1236–1242.
- 47 T. B. Jones, *J. Electrostat.*, 2001, **51**, 290–299.
- 48 V. Vespini, S. Coppola, M. Todino, M. Paturzo, V. Bianco, S. Grilli and P. Ferraro, *Lab Chip*, 2016, **16**, 326–333.